



ARRICCI

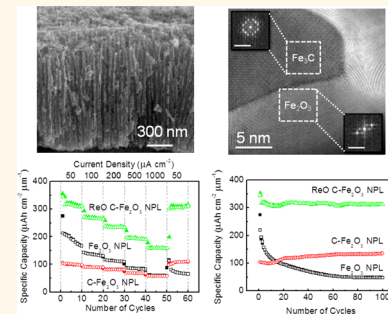
# Three-Dimensional Nanoporous Fe<sub>2</sub>O<sub>3</sub>/Fe<sub>3</sub>C-Graphene Heterogeneous Thin Films for Lithium-Ion Batteries

Yang Yang,<sup>†,‡,§,#</sup> Xiujun Fan,<sup>†,‡,||,§,#</sup> Gilberto Casillas,<sup>†</sup> Zhiwei Peng,<sup>†</sup> Gedeng Ruan,<sup>†</sup> Gunuk Wang,<sup>†,‡</sup> Miguel Jose Yacaman,<sup>†</sup> and James M. Tour<sup>†,‡,§,\*</sup>

<sup>†</sup>Department of Chemistry, <sup>‡</sup>Smalley Institute for Nanoscale Science and Technology, and <sup>§</sup>Department of Materials Science and NanoEngineering, Rice University, 6100 Main Street, Houston, Texas 77005, United States, <sup>||</sup>Department of Physics and Astronomy, University of Texas at San Antonio, One UTSA Circle, San Antonio, Texas 78249, United States, and <sup>||</sup>Beijing University of Technology, College of Electronic Information and Control Engineering, Beijing 100124, China.

#Y. Yang and X. Fan contributed equally to this work.

**ABSTRACT** Three-dimensional self-organized nanoporous thin films integrated into a heterogeneous Fe<sub>2</sub>O<sub>3</sub>/Fe<sub>3</sub>C-graphene structure were fabricated using chemical vapor deposition. Few-layer graphene coated on the nanoporous thin film was used as a conductive passivation layer, and Fe<sub>3</sub>C was introduced to improve capacity retention and stability of the nanoporous layer. A possible interfacial lithium storage effect was anticipated to provide additional charge storage in the electrode. These nanoporous layers, when used as an anode in lithium-ion batteries, deliver greatly enhanced cyclability and rate capacity compared with pristine Fe<sub>2</sub>O<sub>3</sub>: a specific capacity of 356  $\mu\text{Ah cm}^{-2} \mu\text{m}^{-1}$  (3560  $\text{mAh cm}^{-3}$  or  $\sim 1118 \text{ mAh g}^{-1}$ ) obtained at a discharge current density of 50  $\mu\text{A cm}^{-2}$  ( $\sim 0.17 \text{ C}$ ) with 88% retention after 100 cycles and 165  $\mu\text{Ah cm}^{-2} \mu\text{m}^{-1}$  (1650  $\text{mAh cm}^{-3}$  or  $\sim 518 \text{ mAh g}^{-1}$ ) obtained at a discharge current density of 1000  $\mu\text{A cm}^{-2}$  ( $\sim 6.6 \text{ C}$ ) for 1000 cycles were achieved. Meanwhile an energy density of 294  $\mu\text{Wh cm}^{-2} \mu\text{m}^{-1}$  (2.94  $\text{Wh cm}^{-3}$  or  $\sim 924 \text{ Wh kg}^{-1}$ ) and power density of 584  $\mu\text{W cm}^{-2} \mu\text{m}^{-1}$  (5.84  $\text{W cm}^{-3}$  or  $\sim 1834 \text{ W kg}^{-1}$ ) were also obtained, which may make these thin film anodes promising as a power supply for micro- or even nanosized portable electronic devices.



**KEYWORDS:** heterogeneous structure · nanoporous · lithium-ion battery · thin film · anode

To meet the growing demand for portable electronic devices, the development of advanced electrodes for micro- or even nanosized Li-ion batteries (LIBs) with high power and energy density, long-term cyclability, and minimized size,<sup>1–3</sup> such as thin film electrodes,<sup>4–6</sup> is under consideration.<sup>4–6</sup> In principle, a self-organized metal oxide nanoporous layer (NPL) would be more useful than its three-dimensional (3-D) counterparts as thin film electrodes since they have higher surface areas.<sup>7–10</sup> Furthermore, the 3-D open frameworks in the porous structure have the ability to facilitate ion and mass transport and release mechanical stress during Li-ion insertion/extraction cycling, and their superior thermal stability and increased heat transfer ability are factors favoring their use over commercial LIBs.<sup>11–14</sup>

Apart from optimizing LIB performance by structural modification, designing new materials to replace those used commercially is an area of intense research.<sup>15–18</sup>

Metal oxides, especially Fe<sub>2</sub>O<sub>3</sub>, have been extensively regarded as an attractive anode material due to their low toxicity and cost coupled with their high theoretical capacity of 1005  $\text{mAh g}^{-1}$  based on a maximum uptake of 6Li/Fe<sub>2</sub>O<sub>3</sub>.<sup>19</sup> However, one of the commonly encountered challenges in using metal oxides, including Fe<sub>2</sub>O<sub>3</sub> for LIBs, is the severe volume change during Li-ion insertion/extraction cycling along with the detachment of active materials from the current collector. That generally leads to a large initial capacity loss (ICL), low rate capacity, and poor cyclability.<sup>20</sup> Simply decreasing the crystallite size to the nanoscale is not enough to overcome these problems because the larger surface area exposed to the electrolyte and higher surface energy of the nanoscale material make it easier to decompose the electrolyte during the initial discharge/charge cycles.<sup>21</sup> Recently, approaches to form passivation coatings such as core–shell structures and carbon

\* Address correspondence to tour@rice.edu.

Received for review February 12, 2014 and accepted March 26, 2014.

Published online March 27, 2014  
10.1021/nn500865d

© 2014 American Chemical Society

coatings or reduce the charge transfer resistance have been designed to improve the cyclability and rate capacity.<sup>22,23</sup> Furthermore, the use of heterogeneous composites of electrochemically active metal oxides with inactive metal nitrides achieved a synergistic improvement in the LIB performance.<sup>24</sup> The electrochemically inactive components have high hardness to provide structural integrity to the active material, thereby improving capacity retention.<sup>25</sup> However, the improvement of LIB performance by forming  $\text{Fe}_2\text{O}_3/\text{Fe}_3\text{C}$  heterogeneous structures, especially integrated in self-organized 3-D nanostructures covered by few-layer graphene, has not yet been reported. In the present work, a  $\text{Fe}_2\text{O}_3/\text{Fe}_3\text{C}$ -graphene heterogeneous structure was fabricated into a 3-D nanoporous thin film; the following advantages are expected from this advanced anode material for LIBs: (1) the 3-D nanoporous structure provides open channels for lithium-ion transport and storage; (2) conductive graphene layers introduced into the heterogeneous structure should enhance the electrical conductivity of the electrode; (3) the electrochemically inactive  $\text{Fe}_3\text{C}$  phase improves the capacity retention owing to its high hardness; (4) the electrochemically active  $\text{Fe}_2\text{O}_3$  phase with a high theoretical capacity should form a heterogeneous interface with  $\text{Fe}_3\text{C}$  that provides the ability to store additional charge.<sup>26</sup> Therefore, the  $\text{Fe}_2\text{O}_3/\text{Fe}_3\text{C}$ -graphene heterogeneous thin film with a 3-D nanoporous structure could reduce the ICL, improve the rate capacity and the cycling stability of  $\text{Fe}_2\text{O}_3$ .

Chemical vapor deposition (CVD) is generally considered an appropriate method to fabricate micro-devices, thin films, and high-quality two-dimensional layers such as graphene,  $\text{MoS}_2$ , and BN.<sup>27,28</sup> Even though some aspects such as high cost and low yield rate need to improve before using this technique industrially, CVD is a fundamentally excellent method to fabricate thin film electrodes, especially when high-quality graphene layers are needed.<sup>29</sup> It is known that metallic iron is a common catalyst in growing graphene layers or carbon nanotubes due to the high carbon solubility under CVD conditions.<sup>30–32</sup> However, it is still a challenge to form few-layer graphene (FLG) by CVD on the surface of a self-organized  $\text{Fe}_2\text{O}_3$  NPL without the destruction of their well-defined nanostructures, and there has been no report on the CVD growth and energy storage applications of an FLG-coated heterogeneous  $\text{Fe}_2\text{O}_3/\text{Fe}_3\text{C}$  NPL. Here, we report the growth of FLG on an  $\text{Fe}_2\text{O}_3$  NPL, simultaneously forming a heterogeneous  $\text{Fe}_2\text{O}_3/\text{Fe}_3\text{C}$  structure, by low-temperature CVD (for the fabrication process, see the Experimental Section and Figure S1).

## RESULTS AND DISCUSSION

An FLG-coated  $\text{Fe}_2\text{O}_3$  NPL ( $\text{C}-\text{Fe}_2\text{O}_3$  NPL) was fabricated by CVD from an anodically self-organized  $\text{Fe}_2\text{O}_3$  NPL (average diameter of the channels  $\sim 40$  nm and

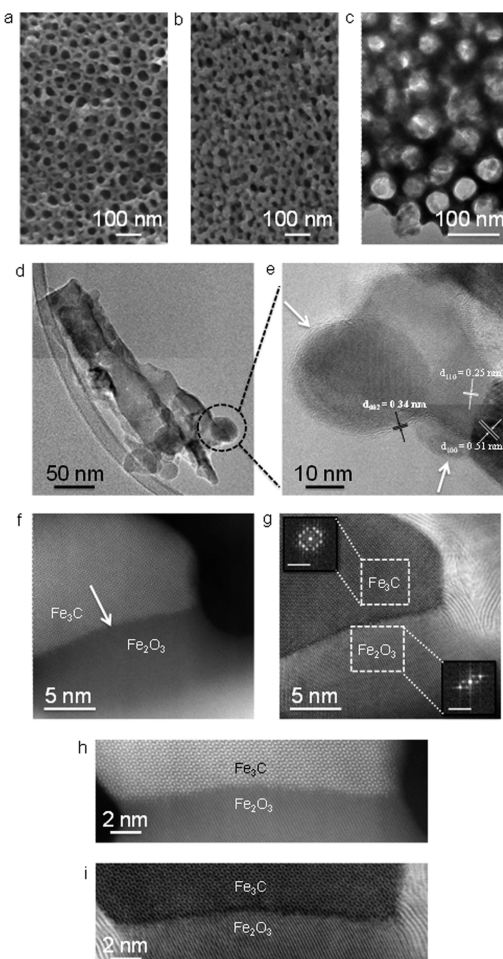


**Figure 1.** Microstructure of the nanoporous layer (NPL). (a and b) SEM images of the NPL before and after forming the heterogeneous structure, respectively. (c) Top-view TEM image of the heterogeneous NPL with the ordered porous structure. (d) Cross-sectional TEM image of the heterogeneous NPL with channel-like morphology. (e) HRTEM image of the heterogeneous structure with FLG shell (highlighted by the arrow). The HRTEM image in (e) was rotated and taken from the circled region marked in (d). (f–i) Atomic-resolution STEM images of the junction of the  $\text{Fe}_2\text{O}_3/\text{Fe}_3\text{C}$  interface boundary (highlighted by the arrow in (f) with the  $\text{Fe}_3\text{C}$  in a [010] zone axis). (f and h) High angle annular dark field images; (g and i) bright field images. Fast Fourier transform (FFT) was performed on the regions marked by white dashed boxes with scale bars being  $10 \text{ nm}^{-1}$ .

length  $\sim 1.2 \mu\text{m}$ ; see Figure 1a and Figure S2). The temperature used for CVD growth of FLG here ( $550^\circ\text{C}$ ) is much lower than conventionally used ( $\sim 850^\circ\text{C}$  with iron particles as catalyst) due to the nanoporous layers that enable faster diffusion and better dissolution of carbon through their ordered channels (Figure S2).<sup>31</sup> Proper postannealing of the  $\text{C}-\text{Fe}_2\text{O}_3$  NPL (reoxidized sample,  $\text{ReO C}-\text{Fe}_2\text{O}_3$  NPL) in air at  $300^\circ\text{C}$  for 1 h was performed to partially convert inactive  $\text{Fe}_3\text{C}$  to electrochemically active  $\text{Fe}_2\text{O}_3$ . The obtained  $\text{ReO C}-\text{Fe}_2\text{O}_3$  NPL maintained its self-organized nanoporous structure (Figure 1b) with slightly increased wall thickness due to the grain growth and new phase formation, whereas attempts to elevate the temperature used

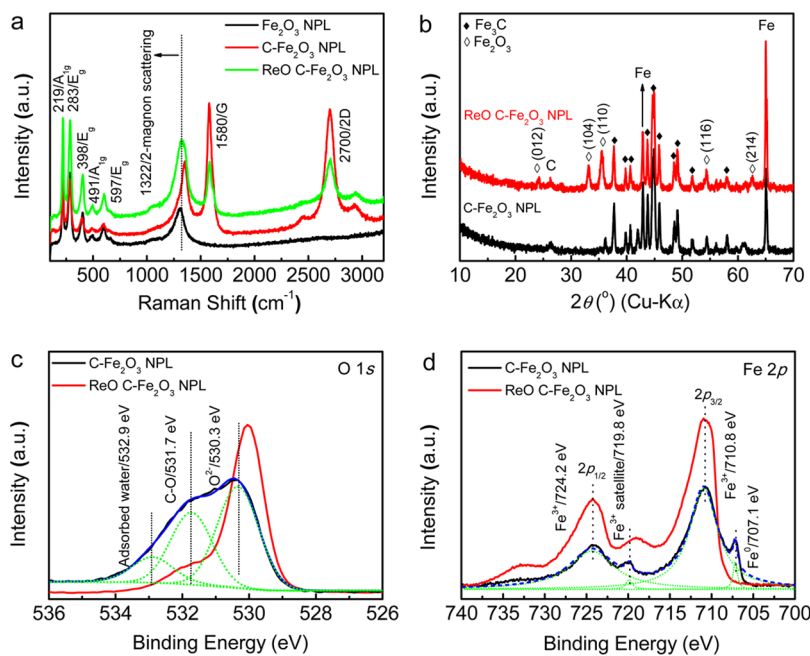


**Figure 2.** Composition analysis of the NPL. (a) Raman spectra of the NPL measured with a 514 nm excitation argon laser. (b) XRD patterns of the heterogeneous NPL before and after postannealing at 300 °C for 1 h. (c and d) XPS O 1s and Fe 2p spectra, respectively. The fitted curves are marked as broken curves in the spectra.

in CVD led to collapse of the ordered nanoporous structure (Figure S3). Samples annealed at lower temperatures show only more graphite-like structure instead of FLG (Figure S4), and more disordered defects were formed in dissolution–precipitation processes (for the potential mechanism of formation of the heterogeneous structure, see Figure S5 and the Supporting Information).<sup>33</sup> TEM observations of a ReO C–Fe<sub>2</sub>O<sub>3</sub> NPL also clearly show that the ordered nanoporous structure from the top (Figure 1c) and channel-like morphology from the cross-section (Figure 1d) were well maintained. The three- to four-layer graphene shell coated on the surface of the NPL was identified from the typical 0.34 nm *d*-spacing that corresponds to the C (002) plane as indicated by the lattice fringes (Figure 1e and Figure S6a,b). Fe<sub>2</sub>O<sub>3</sub> (110) lattice fringes with a *d*-spacing of ~0.25 nm and Fe<sub>3</sub>C (100) planes with lattice fringes of ~0.51 nm are also identified from the NPL, which indicates the formation of the heterogeneous structure. To investigate the junction between Fe<sub>3</sub>C and Fe<sub>2</sub>O<sub>3</sub>, atomic-resolution scanning TEM (STEM) observation was performed on the heterogeneous NPL (Figure 1f–i and Figure S6c,d). It is apparent that Fe<sub>3</sub>C is continuously grown with Fe<sub>2</sub>O<sub>3</sub> under the coating of FLG, and it forms a distinct interface boundary. The formation of an Fe<sub>2</sub>O<sub>3</sub>/Fe<sub>3</sub>C heterogeneous NPL with well-bonded interfaces appears to occur without loss of the FLG coating (Figure 1j).<sup>34</sup> To investigate the porous structure of the NPL thin film, Brunauer–Emmett–Teller (BET) analysis by adsorption/desorption of nitrogen gas was performed. The data were used to determine the Barrett–Joyner–Halenda (BJH) pore size. Nanoscale pores were distributed mainly in a range from 2 to 40 nm (Figure S7).

From the Raman spectra of the samples (Figure 2a), typical bands for Fe<sub>2</sub>O<sub>3</sub> at 219, 283, 398, 491, and 597 cm<sup>-1</sup>, as well as graphene bands at 1580 and 2700 cm<sup>-1</sup>, were identified.<sup>19,35</sup> From the intensity ratio of the G/2D bands (1.046), three- to four-layer graphene was formed,<sup>35</sup> which is consistent with the HRTEM observations. However, a difference was apparent in the 1300 to 1400 cm<sup>-1</sup> range of the samples before and after annealing. The Raman band at ~1322 cm<sup>-1</sup> was from magnon scattering in Fe<sub>2</sub>O<sub>3</sub>, whereas the band at 1350 cm<sup>-1</sup> was assigned to the dissolved carbon (graphite) in the Fe<sub>3</sub>C phase. From the X-ray diffraction (XRD) patterns (Figure 2b) the diffraction peaks for Fe<sub>3</sub>C (PDF #00-035-0772) along with a carbon peak (PDF #04-014-0362) at ~26° are identified. After postannealing treatment on the sample in air, Fe<sub>2</sub>O<sub>3</sub> (α-phase, PDF #00-033-0664) is also distinguished, indicating the formation of a polycrystalline Fe<sub>2</sub>O<sub>3</sub>/Fe<sub>3</sub>C heterogeneous structure. The observed Fe peaks in both samples were from the iron foils that were used as substrates to grow the thin films. A semiquantitative estimate from the XRD pattern indicates the heterogeneous thin film is composed of ~9 wt % carbon, ~24 wt % Fe<sub>2</sub>O<sub>3</sub>, and ~67 wt % Fe<sub>3</sub>C. X-ray photoelectron spectroscopy (XPS) shows clear changes in Fe 2p and O 1s spectra (Figure 2c,d and Figure S8), which indicates the conversion from Fe<sub>3</sub>C to Fe<sub>2</sub>O<sub>3</sub> by postannealing.

To evaluate the LIB performance of the nanoporous thin film anode without overestimation, the specific capacity, energy density, and power density were calculated by area capacity (divided by thin film geometrical area and thickness), volumetric capacity, and gravimetric capacity. Cyclic voltammograms (CVs) were

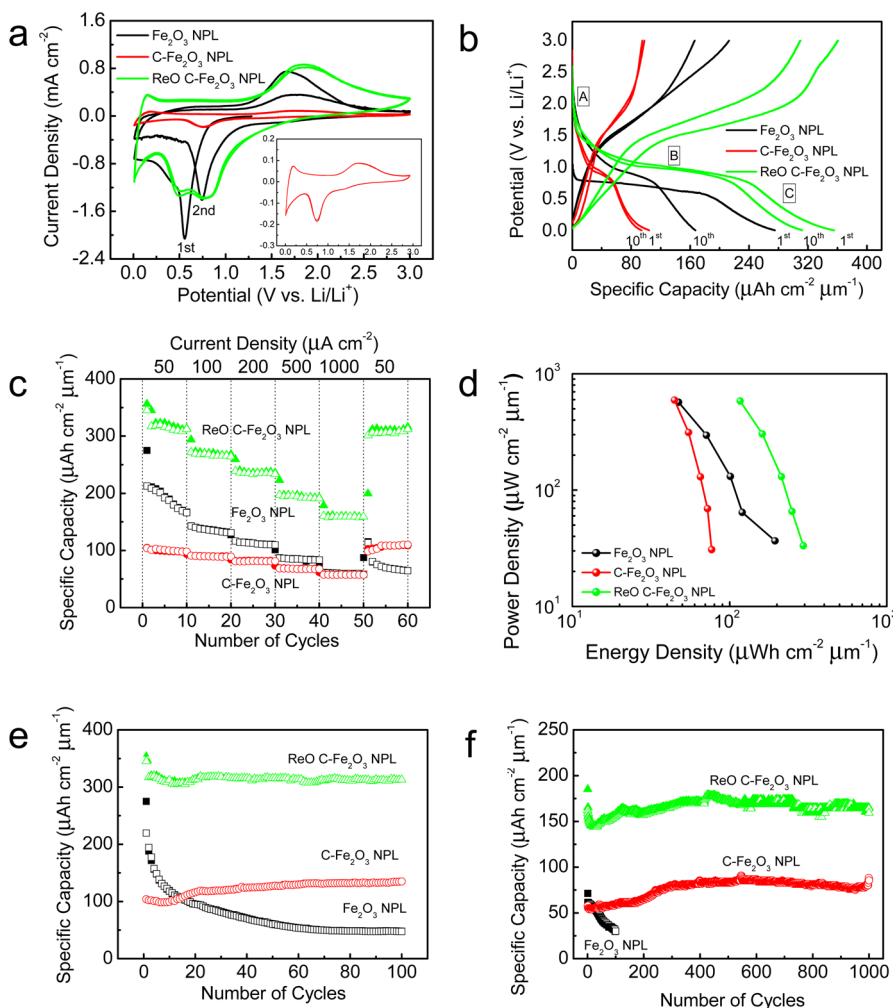


**Figure 3.** Electrochemical performance of the nanoporous thin film for Li-ion batteries. (a) CVs performed over a potential window of 0.01 to 3 V (vs Li/Li<sup>+</sup>) at a scan rate of 0.5 mV s<sup>-1</sup>. The current density was estimated by the geometrical area of the anodes, 0.785 cm<sup>2</sup> in this work. The enlarged CV of C-Fe<sub>2</sub>O<sub>3</sub> NPL is shown in the inset. (b) Galvanostatic discharge/charge curves for the initial 10 cycles at 50 μA cm<sup>-2</sup>. (c) Capacity obtained at different current densities from 50 to 1000 μA cm<sup>-2</sup>. (d) Ragone plot. (e and f) Cycling tests measured at 50 μA cm<sup>-2</sup> for 100 cycles and 1000 μA cm<sup>-2</sup> for 1000 cycles, respectively. The solid and hollow symbols in (c), (e), and (f) denote discharge and charge, respectively.

taken of the samples within a potential window between 0.01 and 3 V (vs Li/Li<sup>+</sup>) at a scan rate of 0.5 mV s<sup>-1</sup> to investigate the electrochemical reactions that occur during the initial two Li-ion insertion/extraction cycles (Figure 3a). By assigning the cathodic and anodic peaks to the redox reactions (see Supporting Information), Li-ion insertion/extraction reactions are identified:  $\text{Fe}_2\text{O}_3 + 6 \text{Li}^+ + 6 \text{e}^- \rightleftharpoons 2 \text{Fe} + 3 \text{Li}_2\text{O}$  (lithium-rich phase).<sup>19</sup>

Galvanostatic discharge/charge tests were performed within a potential window from 0.01 to 3 (V vs Li/Li<sup>+</sup>), a window conventionally used for Fe<sub>2</sub>O<sub>3</sub> anodes,<sup>19,20</sup> at a current density of 50 μA cm<sup>-2</sup> for 10 cycles (Figure 3b) and other current densities up to 1000 μA cm<sup>-2</sup> (Figure 3c; the correspondence between applied current densities and C-rates is listed in Table S1). It was found that the capacity of the pristine Fe<sub>2</sub>O<sub>3</sub> NPL showed a continuous decay throughout the tests and a rapid capacity drop at high current densities: 275 μAh cm<sup>-2</sup> μm<sup>-1</sup> (2750 mAh cm<sup>-3</sup> or ~864 mAh g<sup>-1</sup>)

at 50 μA cm<sup>-2</sup> and 62 μAh cm<sup>-2</sup> μm<sup>-1</sup> (620 mAh cm<sup>-3</sup> or ~195 mAh g<sup>-1</sup>) at 1000 μA cm<sup>-2</sup>, indicating a large ICL and poor rate performance. After coating with graphene, C-Fe<sub>2</sub>O<sub>3</sub> NPLs deliver a capacity of 105 μAh cm<sup>-2</sup> μm<sup>-1</sup> (1050 mAh cm<sup>-3</sup> or ~330 mAh g<sup>-1</sup>) with 90% retention, whereas after postannealing ReO C-Fe<sub>2</sub>O<sub>3</sub> NPLs have an enhanced capacity of 356 μAh cm<sup>-2</sup> μm<sup>-1</sup> (3560 mAh cm<sup>-3</sup> or ~1118 mAh g<sup>-1</sup>) with 88% retention after 10 discharge/charge cycles at 50 μA cm<sup>-2</sup>. Greatly improved electrical conductivity was achieved by the passivation of Fe<sub>2</sub>O<sub>3</sub> NPL through a conductive FLG protective shell. The C-Fe<sub>2</sub>O<sub>3</sub> NPL shows an improved rate performance, with a capacity of 58 μAh cm<sup>-2</sup> μm<sup>-1</sup> (580 mAh cm<sup>-3</sup> or ~182 mAh g<sup>-1</sup>) at a current density of 1000 μA cm<sup>-2</sup>, and it delivers an increased capacity of 109 μAh cm<sup>-2</sup> μm<sup>-1</sup> (1090 mAh cm<sup>-3</sup> or ~343 mAh g<sup>-1</sup>) when the current is reduced back to 50 μA cm<sup>-2</sup>. After postannealing, ReO C-Fe<sub>2</sub>O<sub>3</sub> NPL demonstrated a greatly improved rate performance with a capacity of

$160 \mu\text{Ah cm}^{-2} \mu\text{m}^{-1}$  ( $1600 \text{ mAh cm}^{-3}$  or  $\sim 503 \text{ mAh g}^{-1}$ ) at  $1000 \mu\text{A cm}^{-2}$  as well as a recovered capacity of  $315 \mu\text{Ah cm}^{-2} \mu\text{m}^{-1}$  ( $3150 \text{ mAh cm}^{-3}$  or  $\sim 990 \text{ mAh g}^{-1}$ ) when the current goes back to  $50 \mu\text{A cm}^{-2}$ . The advantages of FLG coating can also be assessed by analysis of the changes in discharge profiles during cycling and the contribution from different lithium storage processes (Figure S9). The enhanced capacity of the ReO C– $\text{Fe}_2\text{O}_3$  NPL compared to the C– $\text{Fe}_2\text{O}_3$  NPL is due to the partial recovery of the electrochemically active  $\text{Fe}_2\text{O}_3$  from inactive  $\text{Fe}_3\text{C}$  after postannealing. As for the increased capacity of the ReO C– $\text{Fe}_2\text{O}_3$  NPL compared to the pristine  $\text{Fe}_2\text{O}_3$  NPL, lithium storage in FLG and synergies in the  $\text{Fe}_2\text{O}_3/\text{Fe}_3\text{C}$ -graphene heterogeneous structure are considered to contribute to the higher capacity.<sup>36,37</sup> Moreover, a possible interfacial lithium storage effect introduced by the formation of the  $\text{Fe}_2\text{O}_3/\text{Fe}_3\text{C}$  interface may also contribute to the higher capacity.<sup>38</sup> One of the common causes of the ICL is from the side reaction of electrolyte decomposition at the electrochemically active surface of the materials. This becomes even more pronounced in nanoscale materials due to their high electrochemically active surface areas.<sup>17</sup> By partially converting from the electrochemically active  $\text{Fe}_2\text{O}_3$  phase to the  $\text{Fe}_3\text{C}$  phase, as well as by forming graphene on the surface as a passivation layer, the electrochemically active area exposed to the electrolyte is decreased. This reduces the ICL. Additionally the hard  $\text{Fe}_3\text{C}$  in the heterogeneous structure maintains its structural integrity. This minimizes detachment between the active materials and the current collector, further reducing the ICL. Considering the thickness of the film used for the tests here ( $\sim 1.2 \mu\text{m}$ ), the capacities obtained in this work are larger than those for most of the state-of-the-art 3-D thin film batteries (Table S2). More interesting is that the nanoporous layers are located in the high power/energy region of the Ragone plot (Figure 3d), which indicates the superior power supply capability of these thin film electrodes. Especially, the ReO C– $\text{Fe}_2\text{O}_3$  NPL shows an energy density up to  $294 \mu\text{Wh cm}^{-2} \mu\text{m}^{-1}$  ( $2.94 \text{ Wh cm}^{-3}$  or  $\sim 924 \text{ Wh kg}^{-1}$ ) and a power density of  $584 \mu\text{W cm}^{-2} \mu\text{m}^{-1}$  ( $5.84 \text{ W cm}^{-3}$  or  $\sim 1834 \text{ W kg}^{-1}$ ), which demonstrates more than an order of magnitude enhanced energy storage performance compared to most published values for 3-D thin film electrodes.<sup>39</sup> Long-term cyclability tests (Figure 3e) show greatly improved capacity retention from 17% ( $\text{Fe}_2\text{O}_3$  NPL) to 88% (ReO C– $\text{Fe}_2\text{O}_3$  NPL) at  $50 \mu\text{A cm}^{-2}$  for 100 cycles. Especially for the cycling tests at current density of  $1000 \mu\text{A cm}^{-2}$ , the capacity retention is improved from 42% ( $\text{Fe}_2\text{O}_3$  NPL) after 100 cycles to 90% (ReO C– $\text{Fe}_2\text{O}_3$  NPL) after 1000 cycles (Figure 3f). The corresponding Coulombic efficiency plots for Figure 3e,f are provided in Figure S10a,b. It is evident the initial Coulombic efficiency was enhanced due to the reduced ICL from forming heterogeneous structures. For the C– $\text{Fe}_2\text{O}_3$  NPL the capacity even increases by 30% and 43%, at  $50$  and  $1000 \mu\text{A cm}^{-2}$ , respectively.

The gradually increased capacity during discharge/charge cycling has also been found in other nanoscale or porous materials,<sup>40,41</sup> however there is still no clear explanation. Considering the 3-D nanoporous structure of the  $\text{Fe}_2\text{O}_3/\text{Fe}_3\text{C}$ -graphene heterogeneous thin film, possible reasons for the gradually increased capacity are due to either the reduced nanoparticle size (by an electrochemical milling effect), which could expose more electrochemically active sites to the electrolyte, or gradual activation of the active materials in the porous structure during the cycling test.<sup>42</sup> The stabilized capacities delivered over long-term cycling (normalized to the first discharge capacity) are better than other forms of  $\text{Fe}_2\text{O}_3$  reported recently, such as graphene oxide/ $\text{Fe}_2\text{O}_3$  composite (only 60% retention after 50 cycles at  $\sim 0.1 \text{ C}$ )<sup>43</sup> and  $\text{Fe}_2\text{O}_3$  hollow spheres (less than 60% retention after 100 cycles at  $\sim 0.2 \text{ C}$ ).<sup>44</sup> The greatly improved capacity retention, as we expected, is attributed to the hard  $\text{Fe}_3\text{C}$  in the heterogeneous structure that maintains the structural integrity and buffers the severe volume change during Li-ion insertion/extraction cycling.<sup>24,25</sup> Although there is no benefit in decreasing the potential hysteresis of the  $\text{Fe}_2\text{O}_3$  NPL, intrinsic to conversion systems,<sup>21</sup> a much decreased ICL, greatly improved rate performance, and cycling stability are achieved by forming an  $\text{Fe}_2\text{O}_3/\text{Fe}_3\text{C}$ -graphene heterogeneous structure. Moreover, any attempts to convert more of the  $\text{Fe}_3\text{C}$  back to  $\text{Fe}_2\text{O}_3$  by postannealing the C– $\text{Fe}_2\text{O}_3$  NPL at  $300^\circ\text{C}$  for 6 h lowered the capacity retention and lowered the initial Coulombic efficiency (Figure S11).

Nyquist plots (Figure 4a) for the samples measured at the open-circuit potential illustrate a depressed semicircle from high to medium frequency followed by a straight sloping line at the low-frequency end. The correspondence between frequency-dependent impedance and equivalent circuit elements in this work can be logically distinguished after fitting to the equivalent circuit (Figure S12). It is evident that charge transfer resistance ( $R_{ct}$ ) is reduced from  $275.9 \pm 7.8 \Omega$  ( $\text{Fe}_2\text{O}_3$  NPL) to  $135.4 \pm 4.8 \Omega$  (C– $\text{Fe}_2\text{O}_3$  NPL) and  $117.3 \pm 6.9 \Omega$  (ReO C– $\text{Fe}_2\text{O}_3$  NPL) after coating the graphene layers. To demonstrate the electrode kinetics of the samples during Li-ion insertion/extraction reactions, impedance spectra were also measured during discharge/charge cycling (Figure S13). The variations of  $R_{ct}$  and  $Z_w$  (Warburg impedance) at different electrode potentials are illustrated in Figure 4b,c.  $R_{ct}$  of the heterogeneous nanoporous anodes at the same electrode potentials in the discharge and charge process show similar values, an indication of reversible reactions occurring on the electrodes, whereas the significant deviation observed in the pristine  $\text{Fe}_2\text{O}_3$  NPL represents irreversible reactions that are taking place. Moreover, both  $R_{ct}$  and  $Z_w$  of the heterogeneous anodes are substantially reduced when compared to the  $\text{Fe}_2\text{O}_3$  NPL throughout the discharge/charge cycling. The reduced  $R_{ct}$  and  $Z_w$  indicate that by forming a heterogeneous structure charge-transfer and

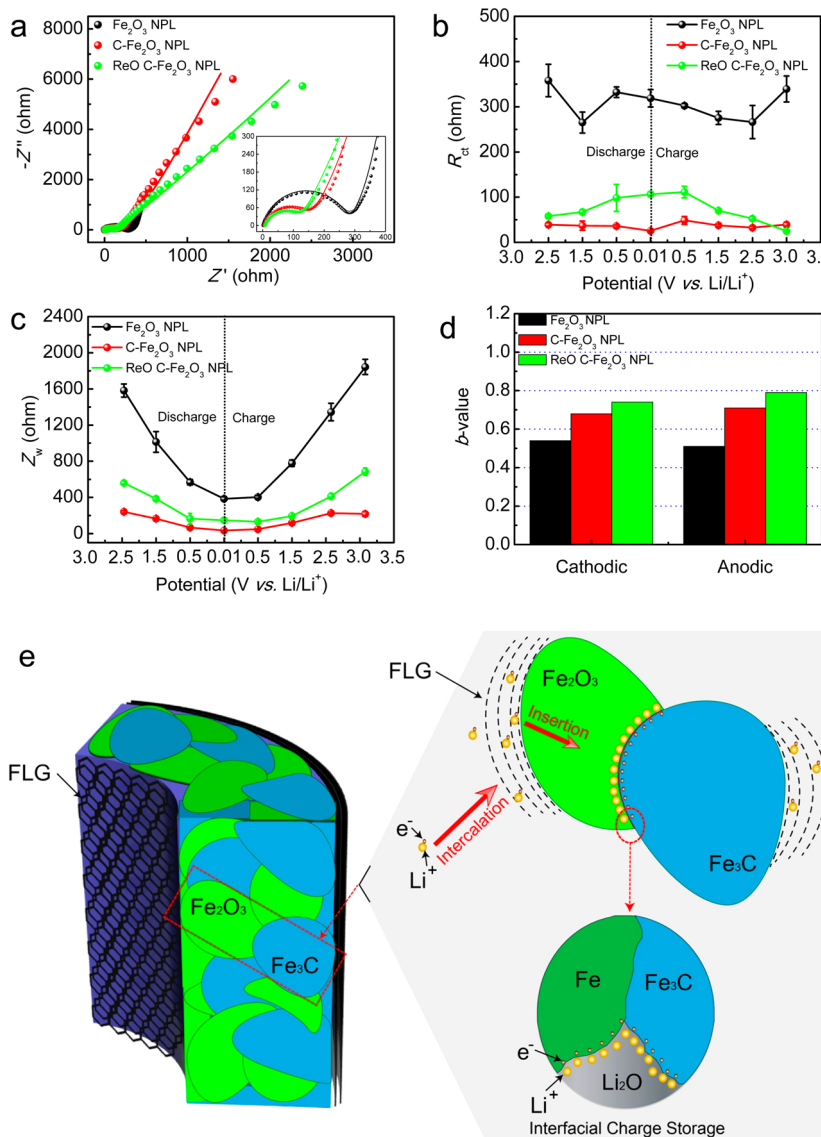


**Figure 4.** Kinetics of the nanoporous thin film anodes and schematic for the interfacial lithium storage mechanism. (a) Nyquist plots of the nanoporous thin film anodes measured at the open-circuit potential. Symbols represent experimental spectra, and continuous lines represent fitted data. (b and c) Variation of  $R_{\text{ct}}$  and  $Z_w$  at different electrode potentials during discharge/charge cycling, respectively. The fitted data were obtained by simulating the EIS spectra with an equivalent circuit. (d) Cathodic and anodic  $b$ -values of the nanoporous anodes. (e) Proposed lithium storage by intercalation into the graphene interlayer and insertion into the lattice of active material, followed by additional charge separation at two-phase boundaries to form space charge layers.

Li-ion diffusion kinetics are improved in the NPL. By measuring the cathodic/anodic peak current changes *vs* the scan rates in CVs, the rate-controlling step of electrode reactions can be identified through calculating the  $b$ -values (Figure S14), which were 0.5 for the diffusion-controlled process and 1 for the surface-controlled process. As shown in Figure 4d, the cathodic and anodic  $b$ -values of the pristine  $\text{Fe}_2\text{O}_3$  NPL are 0.54 and 0.51, respectively, which are close to diffusion-controlled rates. Hence, lithium insertion and diffusion are difficult in the pristine  $\text{Fe}_2\text{O}_3$  NPL, whereas after FLG coating and formation of the heterogeneous structure, the  $b$ -values are more capacitive: 0.68 (cathodic) and 0.71 (anodic) for the  $\text{C}-\text{Fe}_2\text{O}_3$  NPL; 0.74 (cathodic) and 0.79 (anodic) for the  $\text{ReO C}-\text{Fe}_2\text{O}_3$  NPL. After forming the heterogeneous

structure, the graphene coating in the NPL plays an important role in enhancing the electrical conductivity, which reduces the electrode polarization during discharge/charge at high current densities and makes the nanoporous electrode show more capacitive than diffusion-controlled behavior. A possible interfacial lithium storage effect in the oxide/carbide heterogeneous structure is likely responsible for the improved performance of the nanoporous thin film anode (see Figure 4e and Supporting Information).

## CONCLUSION

In summary, a self-organized  $\text{Fe}_2\text{O}_3/\text{Fe}_3\text{C}$ -graphene heterogeneous thin film anode was successfully fabricated by CVD growth. The electrode kinetics during

Li-ion insertion/extraction cycling was greatly improved by forming a graphene protective shell and heterogeneous structure in the thin film. Fe<sub>3</sub>C was introduced to maintain the structural integrity and improve capacity retention during cycling. Possible interfacial lithium storage at the heterogeneous interface by charge separation in space charge layers may also contribute to the enhanced capacity. By this approach a new 3-D heterogeneous nanoporous thin film anode with prominent energy storage capability, *i.e.*, capacity of 356  $\mu\text{Ah cm}^{-2}\mu\text{m}^{-1}$  (3560  $\text{mAh cm}^{-3}$  or  $\sim 1118 \text{ mAh g}^{-1}$ )

at 50  $\mu\text{A cm}^{-2}$  (0.17 C), 160  $\mu\text{Ah cm}^{-2}\mu\text{m}^{-1}$  (1600  $\text{mAh cm}^{-3}$  or  $\sim 503 \text{ mAh g}^{-1}$ ) at 1000  $\mu\text{A cm}^{-2}$  (6.6 C), energy density of 294  $\mu\text{Wh cm}^{-2}\mu\text{m}^{-1}$  (2.94  $\text{Wh cm}^{-3}$  or  $\sim 924 \text{ Wh kg}^{-1}$ ), and power density of 584  $\mu\text{W cm}^{-2}\mu\text{m}^{-1}$  (5.84  $\text{W cm}^{-3}$  or  $\sim 1834 \text{ W kg}^{-1}$ ), is achieved. Cycling tests show that the advanced nanoporous thin film anodes maintain their good performance at different current densities. Taken together, these properties are a harbinger of important advances in thin-film rechargeable batteries.

## EXPERIMENTAL SECTION

**Fabrication.** Iron foils (0.05 mm, 99.5%, Advent Materials, UK) were used as substrates and were cleaned and degreased by sonication in 2-propanol ( $\geq 99.7\%$ , Sigma-Aldrich, USA) and acetone ( $\geq 99.9\%$ , Sigma-Aldrich, USA) before use. Electrochemical anodic treatment was carried out at room temperature in a solution of 0.1 M NH<sub>4</sub>F ( $\geq 98\%$ , Sigma-Aldrich, USA) with 1 M deionized water in ethylene glycol (Fisher Scientific, USA) to grow iron oxide nanoporous layers on the iron substrates. Anodization was conducted at 40 V for 20 min in a two-electrode setup with platinum foil as a counter electrode. To grow thicker layers, extended growth duration is suggested. After that, the samples were immersed in ethanol overnight to remove the residual organic electrolyte in the nanoporous layer followed by annealing at 300 °C for 3 h in air. To form the heterogeneous structure, a CVD apparatus was used. The samples were partially reduced at 300 °C for 30 min in a reducing atmosphere composed of H<sub>2</sub> (200 standard cubic centimeters per minute, sccm)/Ar (200 sccm) at 6.4 Torr followed by CVD growth at 550 °C for 15 min in H<sub>2</sub> (200 sccm)/C<sub>2</sub>H<sub>2</sub> (2 sccm) at 6.4 Torr. During the CVD growth process, H<sub>2</sub>O was supplied by bubbling H<sub>2</sub> throughout degassed water at 200 sccm to remove the amorphous carbon. After that, the nanoporous layers were postannealed at 300 °C for 1 h in air.

**Characterization.** A JEOL 6500F scanning electron microscope (SEM) was used to investigate the morphology of the samples. A JEOL 2010 high-resolution transmission electron microscope (HRTEM) was used to observe the morphologies and lattice fringes of the samples. Atomic-resolution scanning TEM images were recorded by a probe Cs-corrected JEOL JEM-ARM 200F operated at 80 kV. All STEM images were acquired with an exposure time of 31  $\mu\text{s}$  dwell time and a convergence angle of 25 mrad, resulting in a probe size of about 0.08 nm and a current of 22 pA. High-angle annular dark field images were acquired with an inner collection angle of 50 mrad and outer collection angle of 180 mrad. Bright field STEM images were acquired with a collection angle of 11 mrad. The Raman spectra were recorded with a Renishaw Raman RE01 scope (Renishaw Inc., USA) using a 514 nm excitation argon laser. Pore distribution of the NPL was investigated by the BET technique (Quantachrome Autosorb-3B surface analyzer). A 20 mg sample was dried at 130 °C under vacuum (20 mTorr) for 17 h before the test. The crystal structure of the sample was evaluated using X-ray diffraction analysis, which was performed by a Rigaku D/Max Ultima II (Rigaku Corporation, Japan) configured with Cu K $\alpha$  radiation, graphite monochromator, and scintillation counter. A semiquantitative estimation of the composition of the heterogeneous thin film was performed by MDI Jade 9 software. An investigation on the composition and chemical states of the anodic layers was obtained from XPS (PHI Quanta XPS, Physical Electronics, USA).

**Electrochemical Measurement.** The nanoporous layers on iron foil were used directly as working electrodes without adding additives such as binder, current collector, or conducting carbon. The geometrical area of the electrode was 1 cm in diameter ( $\sim 0.785 \text{ cm}^2$ ), and the mass of the electrode was found to be  $\sim 0.3$  mg (measured based on the entire films) for

each piece. Coin cells (CR2032, MTI Corporation, USA) were assembled in an argon-filled glovebox (VAC NEXUS, USA) with both moisture and oxygen content  $< 1.5$  ppm, using Li-metal foil (0.38 mm thick; 99.9%, Sigma-Aldrich, USA) as both the counter and reference electrodes, 1 M LiPF<sub>6</sub> in ethylene carbonate, dimethyl carbonate, and diethyl carbonate (1:1:1 vol %, MTI Corporation, USA) as the electrolyte, and polypropylene foil (Celgard, USA) as the separator. After assembling, the cells were aged for 12 h before the electrochemical measurements. The discharge/charge cycling tests were performed on a multi-channel battery analyzer (Land, CT2001A). The CVs and EIS measurements were carried out with an electrochemical analyzer (CHI 608D, CH Instruments, USA). The CVs were measured at a scan rate of 0.5 mV s<sup>-1</sup> in a potential window from 0.01 to 3 V (vs Li/Li<sup>+</sup>). The EIS were carried out on fresh cells at open-circuit potentials with a frequency range from 10<sup>5</sup> to 10<sup>-2</sup> Hz with an ac signal amplitude of 5 mV. To investigate the electrode kinetics of the samples, the EIS were also carried out at different potentials (0.01, 0.5, 1.5, 2.5, and 3 V) during discharge/charge cycling. The impedance data were simulated by Z-view software (version 2.2, Scribner Associates, USA) to obtain the fitted Nyquist plots and simulated values for each equivalent circuit element.

**Conflict of Interest:** The authors declare no competing financial interest.

**Acknowledgment.** We thank the Peter M. and Ruth L. Nicholas Post-Doctoral Fellowship of the Smalley Institute for Nanoscale Science and Technology for financial support (Y.Y.). Additional funding was provided by the ONR MURI Program (00006766, N00014-09-1-1066), the AFOSR MURI Program (FA9550-12-1-0035), AFOSR (FA9550-09-1-0581), the National Center for Research Resources (5 G12RR013646-12), NSF-PREM (DMR 0934218), and the National Institute on Minority Health and Health Disparities (G12MD007591) from the National Institutes of Health. Support of the Chinese Scholarship Council (X.F.) and helpful discussions with Prof. Xio Guo, Beijing University of Technology.

**Supporting Information Available:** Experimental details and more discussions. This material is available free of charge via the Internet at <http://pubs.acs.org>.

## REFERENCES AND NOTES

- Tarascon, J.-M.; Armand, M. Issues and Challenges Facing Rechargeable Lithium Batteries. *Nature* **2001**, *414*, 359–367.
- Kang, K.; Meng, Y. S.; Bréger, J.; Grey, C. P.; Ceder, G. Electrodes with High Power and High Capacity for Rechargeable Lithium Batteries. *Science* **2006**, *311*, 977–980.
- Goodenough, J. B.; Park, K.-S. The Li-Ion Rechargeable Battery: A Perspective. *J. Am. Chem. Soc.* **2013**, *135*, 1167–1176.
- Long, J. W.; Dunn, B.; Rolison, D. R.; White, H. S. Three-Dimensional Battery Architectures. *Chem. Rev.* **2004**, *104*, 4463–4492.

5. Chan, C. K.; Peng, H.; Liu, G.; Mcilwrath, K.; Zhang, X. F.; Huggins, R. A.; Cui, Y. High-Performance Lithium Battery Anodes Using Silicon Nanowires. *Nat. Nanotechnol.* **2008**, *3*, 31–35.
6. Magasinski, A.; Dixon, P.; Hertzberg, B.; Kvít, A.; Ayala, J.; Yushin, G. High-Performance Lithium-Ion Anodes Using a Hierarchical Bottom-Up Approach. *Nat. Mater.* **2010**, *9*, 353–358.
7. Martinson, A. B. F.; Elam, J. W.; Hupp, J. T.; Pellin, M. J. ZnO Nanotube Based Dye-Sensitized Solar Cells. *Nano Lett.* **2007**, *7*, 2183–2187.
8. Varghese, O. K.; Paulose, M.; Grimes, C. A. Long Vertically Aligned Titania Nanotubes on Transparent Conducting Oxide for Highly Efficient Solar Cells. *Nat. Nanotechnol.* **2009**, *4*, 592–597.
9. Wang, Y.; Zeng, H. C.; Lee, J. Y. Highly Reversible Lithium Storage in Porous SnO<sub>2</sub> Nanotubes with Coaxially Grown Carbon Nanotube Overlays. *Adv. Mater.* **2006**, *18*, 645–649.
10. Ge, M.; Rong, J.; Fang, X.; Zhou, C. Porous Doped Silicon Nanowires for Lithium Ion Battery Anode with Long Cycle Life. *Nano Lett.* **2012**, *12*, 2318–2323.
11. Bae, S. H.; Karthikeyan, K.; Lee, Y. S.; Oh, I. K. Microwave Self-Assembly of 3D Graphene-Carbon Nanotube-Nickel Nanostructure for High Capacity Anode Material in Lithium Ion Battery. *Carbon* **2013**, *64*, 527–536.
12. Sridhar, V.; Kim, H. J.; Jung, J. H.; Lee, C.; Park, S.; Oh, I. K. Defect-Engineered Three-Dimensional Graphene-Nanotube-Palladium Nanostructures with Ultrahigh Capacitance. *ACS Nano* **2012**, *6*, 10562–10570.
13. Li, N.; Chen, Z.; Ren, W.; Li, F.; Cheng, H. M. Flexible Graphene-Based Lithium Ion Batteries with Ultrafast Charge and Discharge Rates. *Proc. Natl. Acad. Sci. U.S.A.* **2012**, *109*, 17360–17365.
14. Lee, S. H.; Sridhar, V.; Jung, J. H.; Karthikeyan, K.; Lee, Y. S.; Mukherjee, R.; Koratkar, N.; Oh, I. K. Graphene-Nanotube-Iron Hierarchical Nanostructure as Lithium Ion Battery Anode. *ACS Nano* **2013**, *7*, 4242–4251.
15. Che, G.; Lakshmi, B. B.; Fisher, E. R.; Martin, C. R. Carbon Nanotubule Membranes for Electrochemical Energy Storage and Production. *Nature* **1998**, *393*, 346–349.
16. Chung, S.-Y.; Bloking, J. T.; Chiang, Y.-M. Electronically Conductive Phospho-Olivines as Lithium Storage Electrodes. *Nat. Mater.* **2002**, *1*, 123–128.
17. Whittingham, M. S. Lithium Batteries and Cathode Materials. *Chem. Rev.* **2004**, *104*, 4271–4301.
18. Dikin, D. A.; Stankovich, S.; Zimney, E. J.; Piner, R. D.; Dommett, G. H. B.; Evmenenko, G.; Nguyen, S. T.; Ruoff, R. S. Preparation and Characterization of Graphene Oxide Paper. *Nature* **2007**, *448*, 457–460.
19. Reddy, M. V.; Yu, T.; Sow, C.-H.; Shen, Z. X.; Lim, C. T.; Rao, G. V. S.; Chowdari, B. V. R.  $\alpha$ -Fe<sub>2</sub>O<sub>3</sub> Nanoflakes as an Anode Material for Li-Ion Batteries. *Adv. Funct. Mater.* **2007**, *17*, 2792–2799.
20. Chen, J. S.; Zhu, T.; Yang, X. H.; Yang, H. G.; Lou, X. W. Top-Down Fabrication of  $\alpha$ -Fe<sub>2</sub>O<sub>3</sub> Single-Crystal Nanodiscs and Microparticles with Tunable Porosity for Largely Improved Lithium Storage Properties. *J. Am. Chem. Soc.* **2010**, *132*, 13162–13164.
21. Poizot, P.; Laruelle, S.; Grégoire, S.; Dupont, L.; Tarascon, J.-M. Nano-Sized Transition-Metal Oxides as Negative-Electrode Materials for Lithium-Ion Batteries. *Nature* **2000**, *407*, 496–499.
22. Dreyer, W.; Jamnik, J.; Guhlke, C.; Huth, R.; Moškon, J.; Gaberšček, M. The Thermodynamic Origin of Hysteresis in Insertion Batteries. *Nat. Mater.* **2010**, *9*, 448–453.
23. Xue, D.-J.; Xin, S.; Yan, Y.; Jiang, K.-C.; Yin, Y.-X.; Guo, Y.-G.; Wan, L.-J. Improving the Electrode Performance of Ge Through Ge@C Core-Shell Nanoparticles and Graphene Networks. *J. Am. Chem. Soc.* **2012**, *134*, 2512–2515.
24. Hu, Y. S.; Demir-Cakan, R.; Titirici, M. M.; Müller, J. O.; Schlägl, R.; Antonietti, M.; Maier, J. Superior Storage Performance of a Si@SiO<sub>x</sub>/C Nanocomposite as Anode Material for Lithium-Ion Batteries. *Angew. Chem., Int. Ed.* **2008**, *47*, 1645–1649.
25. Patel, P.; Kim, I. S.; Kumta, P. N. Nanocomposites of Silicon/Titanium Carbide Synthesized Using High-Energy Mechanical Milling for Use as Anodes in Lithium-Ion Batteries. *Mater. Sci. Eng., B* **2005**, *116*, 347–352.
26. Mashtalir, O.; Naguib, M.; Mochalin, V. N.; Dall'Agne, Y.; Heon, M.; Barsoum, M. W.; Gogotsi, Y. Intercalation and Delamination of Layered Carbides and Carbonitrides. *Nat. Commun.* **2013**, *4*, 1716.
27. Tour, J. M. Top-Down versus Bottom-Up Fabrication of Graphene-Based Electronics. *Chem. Mater.* **2014**, *26*, 163–171.
28. Gong, Y.; Shi, G.; Zhang, Z.; Zhou, W.; Jung, J.; Gao, W.; Ma, L.; Yang, Y.; Yang, S.; You, G.; Vajtai, R.; Xu, Q.; Macdonald, A. H.; Yakobson, B. I.; Lou, J.; Liu, Z.; Ajayan, P. M. Direct Chemical Conversion of Graphene to Boron- and Nitrogen- and Carbon-Containing Atomic Layers. *Nat. Commun.* **2014**, *5*, 3193.
29. James, D. K.; Tour, J. M. Graphene: Powder, Flakes, Ribbons, and Sheets. *Acc. Chem. Res.* **2013**, *46*, 2307–2318.
30. Ren, Z. F.; Huang, Z. P. Synthesis of Large Arrays of Well-Aligned Carbon Nanotubes on Glass. *Science* **1998**, *282*, 1105–1107.
31. Li, Y.-L.; Kinloch, I. A.; Windle, A. H. Direct Spinning of Carbon Nanotube Fibers from Chemical Vapor Deposition Synthesis. *Science* **2004**, *304*, 276–278.
32. Zhang, C.; Li, J.; Liu, E.; He, C.; Shi, C.; Du, X.; Hauge, R. H.; Zhao, N. Synthesis of Hollow Carbon Nano-Onions and Their Use for Electrochemical Hydrogen Storage. *Carbon* **2012**, *50*, 3513–3521.
33. Öya, A.; Marsh, H. Phenomena of Catalytic Graphitization. *J. Mater. Sci.* **1982**, *17*, 309–322.
34. Kim, H. J.; Runk, R. B. The Characterization of the Thin Oxide Film Formed over Fe<sub>3</sub>C at 300 °C. *Oxid. Met.* **1970**, *3*, 307–318.
35. Ferrari, A. C.; Meyer, J. C.; Scardaci, V.; Casiraghi, C.; Lazzeri, M.; Mauri, F.; Piscanec, S.; Jiang, D.; Novoselov, K. S.; Roth, S.; et al. Raman Spectrum of Graphene and Graphene Layers. *Phys. Rev. Lett.* **2006**, *97*, 187401.
36. Su, L.; Zhou, Z.; Shen, P. Core-Shell Fe@Fe<sub>3</sub>C/C Nanocomposites as Anode Materials for Li Ion Batteries. *Electrochim. Acta* **2013**, *87*, 180–185.
37. Su, Q.; Xie, D.; Zhang, J.; Du, G.; Xu, B. *In Situ* Transmission Electron Microscopy Observation of the Conversion Mechanism of Fe<sub>2</sub>O<sub>3</sub>/Graphene Anode during Lithiation-Delithiation Processes. *ACS Nano* **2013**, *7*, 9115–9121.
38. Maier, J. Thermodynamics of Electrochemical Lithium Storage. *Angew. Chem., Int. Ed.* **2013**, *52*, 4998–5026.
39. Pikul, J. H.; Zhang, H. G.; Cho, J.; Braun, P. V.; King, W. P. High-Power Lithium Ion Microbatteries from Interdigitated Three-Dimensional Bicontinuous Nanoporous Electrodes. *Nat. Commun.* **2013**, *4*, 1732.
40. Du, Y.; Yin, Z.; Zhu, J.; Huang, X.; Wu, X.; Zeng, Z.; Yan, Q.; Zhang, H. A General Method for the Large-Scale Synthesis of Uniform Ultrathin Metal Sulphide Nanocrystals. *Nat. Commun.* **2012**, *3*, 1177.
41. Yu, Y.; Shi, Y.; Chen, C.-H. Nanoporous Cuprous Oxide/Lithia Composite Anode with Capacity Increasing Characteristic and High Rate Capability. *Nanotechnology* **2007**, *18*, 055706.
42. Hassan, M. F.; Guo, Z.; Chen, Z.; Liu, H.  $\alpha$ -Fe<sub>2</sub>O<sub>3</sub> as an Anode Material with Capacity Rise and High Rate Capability for Lithium-Ion Batteries. *Mater. Res. Bull.* **2011**, *46*, 858–864.
43. Zhu, X.; Zhu, Y.; Murali, S.; Stoller, M. D.; Ruoff, R. S. Nanostructured Reduced Graphene Oxide/Fe<sub>2</sub>O<sub>3</sub> Composite as a High-Performance Anode Material for Lithium Ion Batteries. *ACS Nano* **2011**, *4*, 3333–3338.
44. Wang, B.; Chen, J. S.; Wu, H. B.; Wang, Z.; Lou, X. W. Quasiemulsion-Templated Formation of  $\alpha$ -Fe<sub>2</sub>O<sub>3</sub> Hollow Spheres with Enhanced Lithium Storage Properties. *J. Am. Chem. Soc.* **2011**, *133*, 17146–17148.